Control of bending wave reflection at beam terminations by thermally tunable subwavelength resonators

Guillaume Raybaud[a,1], Morvan Ouisse[b], Julien Leng[a], Adrien Pelat[a], Jean-Philippe Groby[a], Vicent Romero-García[a], Rubén Picó[c] and François Gautier[a]

[a]*Laboratoire d'Acoustique de l'Université du Mans (LAUM), UMR CNRS 6613, Institut d'Acoustique - Graduate School (IA-GS), Avenue Olivier Messiaen, 72085 Le Mans, France*

[b]*FEMTO-ST institute, Univ. Bourgogne Franche-Comté, UMR CNRS 6174, Department of Applied Mechanics, 24 Chemin de l'épitaphe, 25000 Besançon, France*

[c]*Instituto para la Gestión Integral de zonas Costeras (IGIC), Universitat Politècnica de València, Paranimf 1, E-46730, Gandia, Spain*

ARTICLE INFO

Keywords:
subwavelength absorber
bending wave
perfect absorption
reflection coefficient
thermal control

ABSTRACT

The perfect absorption of bending waves by thermally tunable subwavelength absorbers is analytically and experimentally demonstrated in this work for a reflection problem in beams. These absorbers are local resonators located at the end of a semi-infinite beam and consist of thin blades covered with a layer of Shape Memory Polymer (SMP), the stiffness and damping of which strongly depend on the temperature. The resonators therefore present both energy leakage from the absorbers to the beam and inherent losses thanks to the presence of the SMP. In particular, the situation in which the inherent losses balances the energy leakage is known as the critical coupling conditions and leads to the perfect absorption of the incident wave in the reflection problem. It is shown that these conditions can be simultaneously fulfilled for the different blades of the resonating system by tuning the temperature of the SMP and the geometry of the blades. The analytical results are based on the Impedance Matrix Method. The experimental validation highlights the possibility of achieving multi-frequency subwavelength absorption in the case of multi-blades configurations.

1. Introduction

In the last decades, a large number of solutions have been proposed for controlling vibrations in structural waveguides. The use of viscoelastic materials is a common and efficient solution to achieve damping over a wide frequency range [1, 2]. In this case, the vibration damping results from heat dissipation obtained with the shear forces in the viscoelastic material. More efficiency in narrow frequency band can be achieved by using local resonators, such as Tuned Vibration Absorbers (TVAs) or Tuned Mass Dampers (TMDs) [3]. These solutions are extensively covered in the literature and consist in trapping the wave energy inside the TVA at a target frequency [4, 5, 6]. A wide variety of designs have been proposed in various contexts to reduce the vibration of target modes (civil engineering, machinery, rolling motion of ships, ship hull vibrations, aircraft vibrations, etc.) [7]. Being often compact, TMDs can also be periodically arranged to decrease the vibrational response of structures by making use of destructive Bragg interferences at specific frequency ranges called bandgaps or stop bands [8, 9, 10, 11, 12].

In the case of a beam like structure, a local sub-wavelength resonator can be practically made by extending the beam with a very thin beam segment, called blade, the first mode frequency of which matches a targeted frequency of interest. The absorption by this kind of system has already been studied in the case of a reflection and transmission problem [13]. Perfect absorption, or zero reflection, occurs when the inherent losses of the resonator exactly compensates the energy that leaks out through the interface between the resonator and the surrounding medium. This phenomenon is called critical coupling [13, 14, 15].

One way to control the inherent losses in the system is to bond a thin layer of damping material to the resonator. However, fulfilling the critical coupling conditions requires to precisely adjust the inherent losses of the system, which is difficult in practice when using conventional damping materials. The damping properties of such materials do not depend only on the type of material used, but also on the way the material is bonded to the structure and on the ambient temperature. Practical conditions can therefore deviate from ideal analytical and numerical conditions. Moreover, the

ORCID(s):
[1]guillaume.raybaud@univ-lemans.fr

modification of the losses in the system implies to change the viscoelastic material which can also be arduous. The investigation of other methods to control more effectively the inherent losses of the resonators is therefore of great interest.

In this work, the possibility of tuning the subwavelength resonator properties by using temperature is investigated. To this end, we use a shape memory polymer (SMP) whose properties strongly depend on temperature. In particular, by increasing the temperature and reaching the glass transition temperature of the SMP, the SMP softens and becomes more dissipative. This particular temperature is localised in the transition state where the material changes from a glassy state to a rubbery state. We use tBA/PEGDMA which has been characterized in previous studies [16] and for which it is possible to precisely adjust the damping of the system by thermal control [17].

The objective of the paper is to demonstrate the possibility of controlling the reflection of the bending waves at the end of a beam by achieving perfect absorption at one or two a priori targeted frequencies. The use of local resonators (single or double blades) critically coupled by thermal control allows such control. This mechanical system constitutes a tunable absorber on given geometry specifications.

Three subwavelength absorber configurations are chosen and presented in Sec. 2. A model to compute the reflection coefficient is developed and used to evaluate the thermal and geometrical tuning in Sec. 3. Then, the experimental results compared to the analytical simulations are shown in Sec. 4.

2. Configuration of the subwavelength absorbers

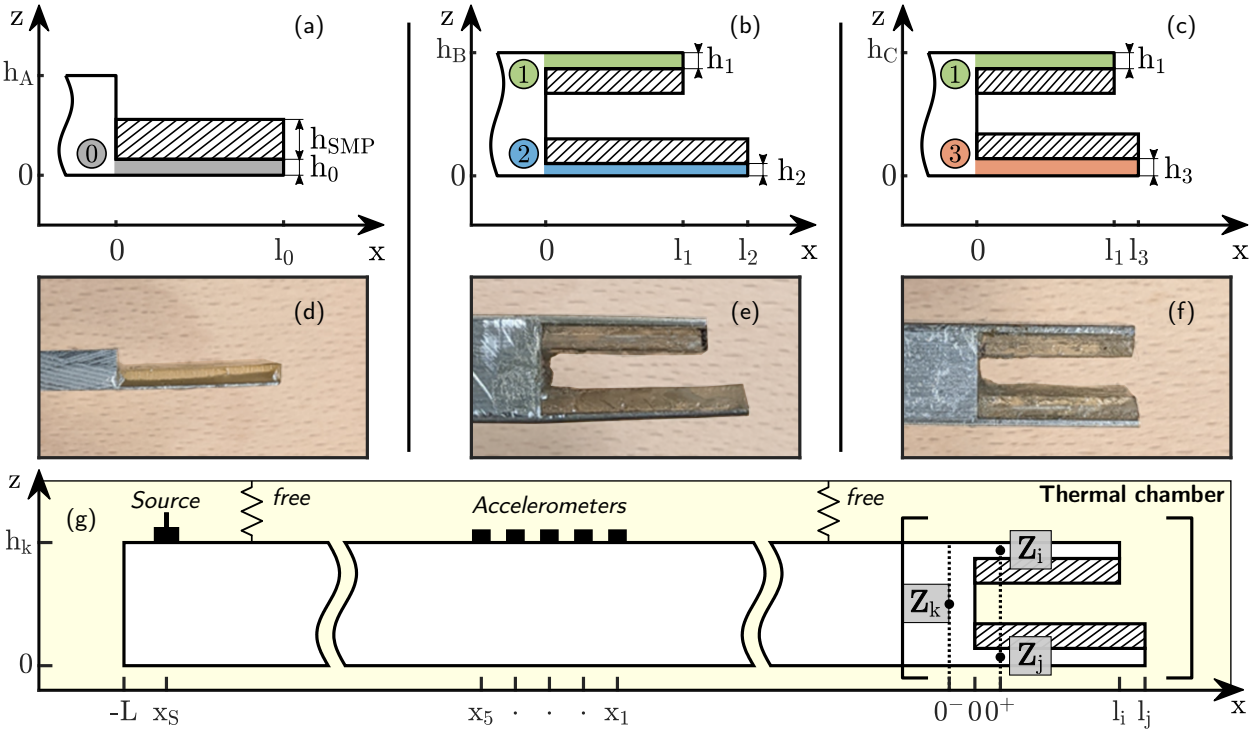

Figure 1: (a) Schematic view of the single-blade (A). (b) Resp. dual-blade (B). (c) Resp. dual-blade (C). The geometry of the blades are reported in Tab. 1. $h_A = 5$ mm, $h_B = h_C = 10$ mm and $h_{SMP} = 2$ mm. (d) Photograph of single-blade (A) realised by wirecut electrical discharge machining. (e) Resp. dual-blade (B). (f) Resp. dual-blade (C). (g) Schematic view of the experiment set-up. The configurations (A), (B), (C), denoted k in a general case, are hung up in a thermal chamber. The reflection coefficient at $x = 0$ is measured using a voice-coil source at x_S about 1 cm from the free edge and 5 accelerometers 25 mm apart halfway between x_S and $x = 0$. The lenghts l_i and l_j denote the length of the blades. $\mathbf{Z}_i$ and $\mathbf{Z}_j$ denote the impedance matrices of the blades at $x = 0^+$ and $\mathbf{Z}_k$ denotes the impedance matrix of the whole system at $x = 0^-$.

The system under study is a structural waveguide subjected to bending waves and consists of an aluminium beam of regular cross section. Blade resonators are placed at the end of the beam. A layer of SMP of thickness $h_{SMP} = 2$ mm is also placed on each blade. These resonators present therefore both inherent losses through the presence of the SMP layers, and energy leakage since the flexural field can propagate from the resonators to the waveguide through the interface connecting the 2 systems and vice-versa [13, 14].

Three configurations are considered (see Fig. 1): a single-blade configuration (A) (see Fig. 1(a)) and two dual-blade configurations with detuned (B) (see Fig. 1(b)) or close (C) resonance frequencies (see Fig. 1(c)). These configurations are realized and photographed in Figs. 1(d), 1(e) and 1(f), respectively.

3. Analytical model of the reflection coefficient of the beam termination

The reflection coefficient is computed using the Impedance Matrix Method which is a convenient method for variable property waveguides [18, 19, 20], adapted from an acoustic context [21]. In the case of blades covered with uniformly heated SMP, the properties of the termination do not depend on the x axis outside the junction. The resolution is then more direct. The Transfer Matrix Method is an alternative method to reach the same result [22].

In the framework of Euler–Bernoulli model for beams in harmonic regime [23], the state vector $\mathbf{X}^{\mathrm{T}} = [w\ \theta\ Q\ M]$ is composed of the displacement w, the slope θ, the shear force Q and the bending moment M. The time convention is chosen to be $e^{-j\omega t}$. The governing equations can be written in the state-space as

$$\frac{\partial \mathbf{X}}{\partial x} = \mathbf{H}\mathbf{X}, \tag{1}$$

with

$$\mathbf{H} = \left[\begin{array}{cc|cc} 0 & 1 & 0 & 0 \\ 0 & 0 & 0 & 1/E^*(\mathrm{T})I \\ \hline -\rho S\omega^2 & 0 & 0 & 0 \\ 0 & 0 & -1 & 0 \end{array}\right] = \begin{bmatrix} \mathbf{H}_1 & \mathbf{H}_2 \\ \mathbf{H}_3 & \mathbf{H}_4 \end{bmatrix}. \tag{2}$$

$\mathbf{H}$ is the transition matrix, which is a compact formulation of the Euler–Bernoulli model, where ω is the angular frequency, ρ is the mass density, S is the beam cross-sectional area and I is the moment of inertia. $E^*(\mathrm{T}) = E(1 + j\eta)$ is the local equivalent complex storage modulus describing the elastic (with the Young's modulus E) and viscous properties (with the loss factor η) of the sandwich beam compound by the aluminium and SMP layers at temperature T. The equivalent parameters of the multi-layer termination are computed in Eq. (2) using the Ross Ungar Kerwin mixing law [24] (see [25]).The impedance matrix $\mathbf{Z}$, which relates the kinematic and the force in $\mathbf{X}$, can be expressed by solving the Riccati equation (see Eq. (A.4) in [18]):

$$\frac{\partial \mathbf{Z}}{\partial x} = -\mathbf{Z}\mathbf{H}_1 - j\omega\mathbf{Z}\mathbf{H}_2\mathbf{Z} + \frac{\mathbf{H}_3}{j\omega} + \mathbf{H}_4\mathbf{Z}. \tag{3}$$

This equation is linear since it does not depend on the x axis for $x < 0$. It can therefore be directly solved from the free end condition at $x = \mathrm{l_i}$ to $x = 0^+$ for each blade i (with i = ⓪, ①, ② or ③).

At the junction (see Fig. 1(g)), the continuity of displacement and slope, and the balance of forces and moments give the following system for one or multiple attached blades:

$$\begin{cases} w(0^-) = w(0^+) \\ \theta(0^-) = \theta(0^+) \\ Q_k(0^-) = \sum_i Q_i(0^+) \\ M_k(0^-) = \sum_i M_i(0^+) \end{cases}. \tag{4}$$

In terms of impedance, these relations can be written in a compact way as a simple impedance addition considering two blades i and j (see Fig. 1(g)):

$$\mathbf{Z}_k(0^-) = \mathbf{Z}_i(0^+) + \mathbf{Z}_j(0^+), \tag{5}$$

where $\mathbf{Z}_i(0^+)$ and $\mathbf{Z}_j(0^+)$ are the impedances of the blades i et j before the junction and $\mathbf{Z}_k(0^-)$ is the impedance of the full termination after the junction (see Fig. 1(g)). The index k denotes the beam configuration (A), (B) or (C).

In order to calculate the reflection matrix $\mathbf{R}$ at $x = 0^-$, the final step consists in switching from the state to the wave formalism, which leads to

$$\mathbf{R} = [j\omega\mathbf{Z}\mathbf{E}_2 - \mathbf{E}_4]^{-1}[\mathbf{E}_3 - j\omega\mathbf{Z}\mathbf{E}_1], \tag{6}$$

where $\mathbf{E}$ is the matrix whose columns are the eigenvectors of $-j\mathbf{H}$ (see Eqs. (A.5) to (A.10) in [18]). Although $\mathbf{R}$ is a matrix whose diagonal components describe the reflection of propagative and evanescent waves, the following sections will focus only on the far-field propagation ($x \to -\infty$). The component R_{11}, which carries the energy and is frequency dependent, is therefore only considered and denoted R in the following.

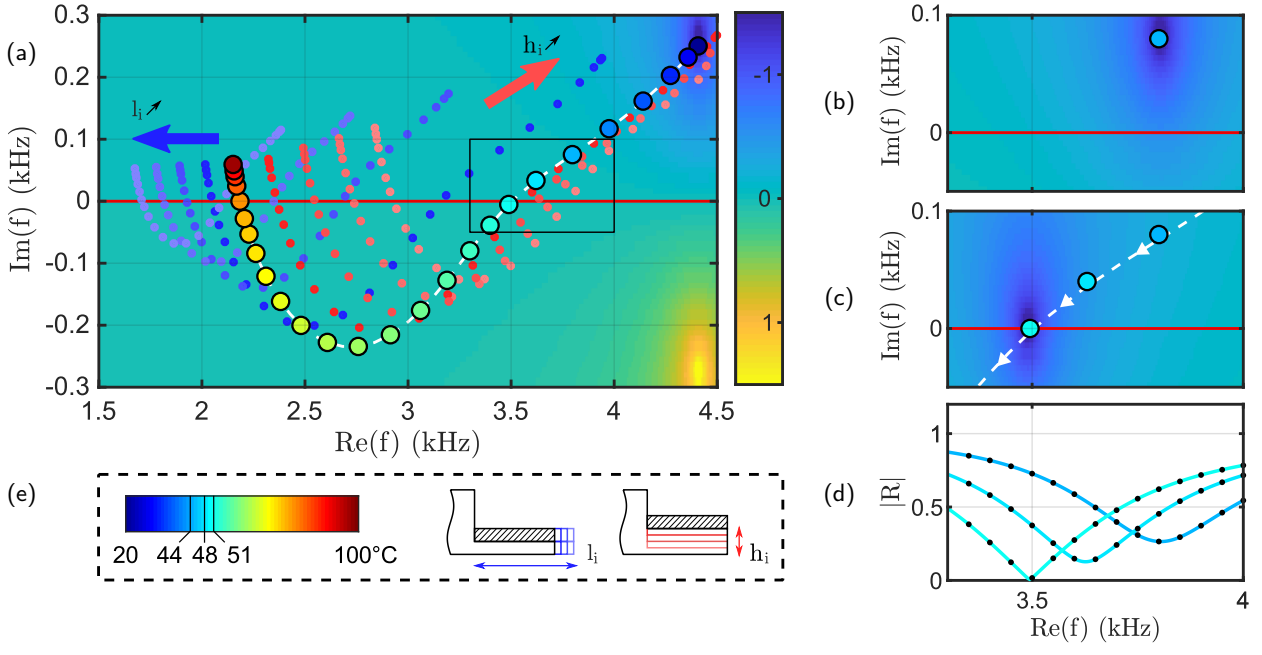

Figure 2: (a) Position of the zero under parametric variation. The variation of temperature is followed by the color marker and the dashed white trajectory. The blue (resp. red) markers correspond to the white trajectory with a variation of length (resp. thickness). The colormap corresponds to log|R| of the nominal configuration at 20°C. The black frame corresponds to the zoom of (b) and (c). (b) Complex frequency plane of log|R| (colormap) of the nominal configuration at 44°C. (c) Complex frequency plane of log|R| of the nominal configuration at 51°C. The white dashed line indicates the trajectory of the zero when the temperature increases. The markers corresponds to the position of the first zero at 44°C, 48°C and 51°C. (d) |R| as function of Re(f) for the 3 temperature configurations at 44°C, 48°C and 51°C corresponding to the markers of (c). (e) Caption block for the parametric variation.

The modulus of R is plotted in Fig. 2(a) in the complex frequency plane for a nominal geometry. This nominal geometry is chosen to be a beam of thickness h = 10 mm extended by the blade (1). The background color map corresponds to log|R| plotted in the complex frequency plane in the case where the system is quasi-conservative with the SMP at room temperature (20°C): at this temperature, the SMP is in a glassy state with a very small loss factor. One pole (yellow spot), for which |R| is singular, can be noticed as well as a zero (blue spot) at a specific complex frequency. The real part of the frequency associated to the pole and zero corresponds to the resonance frequency of

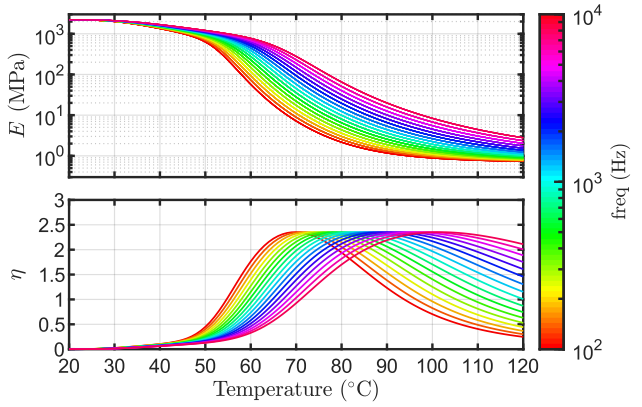

Figure 3: Temperature and frequency dependence of the Young's modulus E and the loss factor η of the shape memory polymer (tBA/PEGDMA) governed by the empirical formula in [16].

the system, whereas the imaginary part corresponds to the amount of losses in the system. In the conservative case, these losses are directly the energy leakage propagating from the blade to the beam. As the time convention is $e^{-j\omega t}$, the frequency of the poles has a negative imaginary part. In a conservative case, the frequency of zeros and poles are complex conjugate due to the temporal invariance property of the scattering matrix. As a consequence, the position of the poles can be controlled by introducing losses into the system. If the losses exactly compensate the leakage, the zero is exactly located on the real frequency axis. This phenomenon is called the critical coupling [14, 15].

The losses and the elastic properties are tuned using a heated layer of SMP. The intrinsic viscoelastic properties of this material are plotted as a function of the temperature and frequency on Fig. 3 [16]. The Young modulus E decreases in a monotonous way with the temperature and rapidly around 70°C at 100 Hz. This fast variation corresponds to the glass transition. The loss factor η increases rapidly up to the glass transition to reach a high value of 2.5, then decreases.

Figures 2(b) and 2(c) show the effect of increasing the losses on the location of the zero in the complex frequency plane. The resulting |R| along the real frequency is also plotted in Fig. 2(d). Figure 2(b) corresponds to the system with losses (heated at 44°C). By increasing the losses, which corresponds to increasing the temperature from 44°C to 48°C then 51°C, the zero can be moved and aligned on the real frequency axis and thus reach the critical coupling (see Fig. 2(c)). Above that temperature, there is too much losses to achieve this goal.

Figure 2(a) depicts the variation of the zero position when the temperature and the geometry of the blade evolve. The white dashed line under the colored markers, the color of which refers to the temperature (see Fig. 2(e)) describes the evolution of the first zero when the temperature increases from 20 to 100°C for the nominal geometry. The shape of the trajectory is in accordance with the intrinsic temperature dependent properties of the SMP: the zero monotonously shifts to the low frequencies when the temperature rises and the losses increase until the glass transition state of the SMP and then decrease. It can be observed that two different temperatures result in locating the zero on the real frequency axis.

Figure 2(a) also shows two other parametric variations on the length l_i and the thickness h_i, see the inset Fig. 2(e). For each increment of the geometric variation, the same temperature variation is applied. The length variation is marked with a set of blue points of different shade. Each shade is an increment of l_i. When l_i increases, the trajectory moves towards the low frequencies by tightening. In a similar way, when the thickness of the beam h_i decreases (set of red points), the trajectory moves towards the high frequencies and towards the positive imaginary frequencies.

This representation provides a deep understanding of the roles played by l_i, h_i and the temperature in the position of the zeros of R. It can be noticed that it is possible to locate a zero on the real frequency axis on a large frequency band by playing with these 3 parameters. By considering the same process for the zeros corresponding to the higher order modes, it is possible to locate a zero on the real frequency axis at very high frequencies. In addition, it is possible to reach very low frequencies by playing with other parameters such as the thickness of the uniform beam (i.e., single-blade (A)).

In the following, it is proposed to build a tool providing the operating temperature that leads to a perfect absorption at a target frequency and for a given resonator geometry. This tool is depicted in Fig. 4, in which a surface gathering all

the configurations of length l_i and thickness h_i that lead to a perfect absorption at a given temperature T and frequency f is represented.

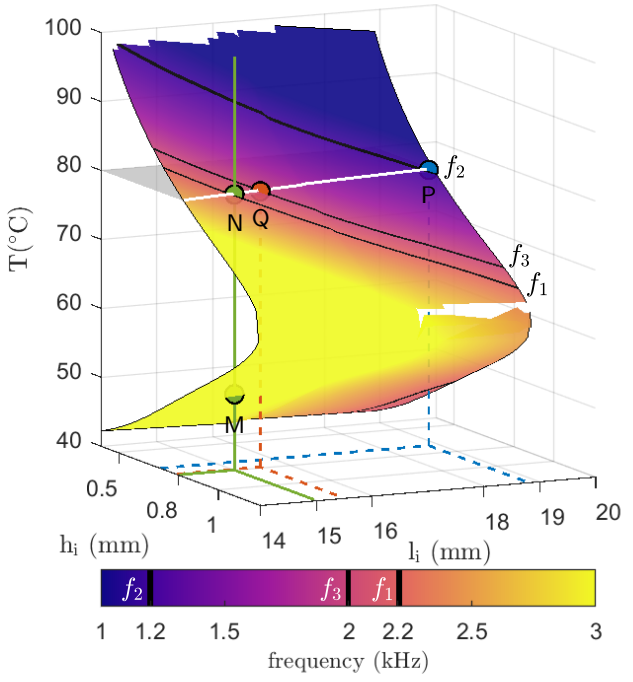

Figure 4: Surface gathering all the configurations of length l_i and thickness h_i leading to a perfect absorption at operating temperature T. The absorption frequency is represented by the colormap. The points M and N are the two critical coupling configurations for a nominal geometry occurring at 51°C and 80°C. The white line represents a chosen temperature of 80°C and the black lines are the isolines of the target frequencies f_1, f_2 and f_3. The points M, P and Q denote the configurations from the temperature and frequency set point which corresponds to the intersection between the white and black lines.

To obtain the surface in Fig. 4, the previous analysis is repeated by varying the temperature and the geometry of the blade. Then, all the configurations that give rise to a critical coupling are stored (i.e., the configurations where the zero is located on the real frequency axis). Finally, these data are organized in the form of a surface with l_i, h_i and T. The color scale indicates the frequency at which $|R| = 0$. This surface can be read as follows: for the nominal geometry $l_i = 15$ mm and $h_i = 0.8$ mm, the vertical line crosses the surface at two points M and N. This means that two critically coupled configurations are found, one at 51°C for 3.5 kHz (point M) and another at 80°C for 2.2 kHz (point N). Referring to Fig. 2(d), the trajectory of the zero intersects twice the real frequency axis at these points. The folding of this surface corresponds to the case where the top of the trajectory of the zero in Fig. 2(a) is tangent to the real frequency axis.

Using this surface, it becomes possible to find the geometrical configurations of blade meeting the critical coupling conditions at the targeted frequencies and fixed temperature. In the case of a SMP temperature fixed at 80°C and targeted frequencies $f_1 = 2.2$ kHz, $f_2 = 1.2$ kHz and $f_3 = 2$ kHz, the configurations for which the critical coupling conditions are met correspond to the intersections of the white and black lines in Fig. 4, and denoted by the point N, P and Q. The geometry and temperature corresponding to these points are given in Tab. 1. The blade (0) has been subjected to the same analysis with a thinner uniform beam in order to reach lower frequencies.

4. Numerical and experimental application

The systems (A), (B), (C), represented in Figs. 1(a),(b),(c), are designed from the previous study. The single-blade (A) has a thickness of $h_A = 5$ mm and is ended by the blade denoted (0). The dual-blades are thicker, $h_B = h_C = 10$ mm, for manufacturing reasons, and are ended by the blades (1) and (2) for the configuration (B) and the blades (1) and

Table 1
Geometry, target frequency and operating temperature for each blade.

Blade	①	②	③	④
l_i (mm)	20	15	18.8	15.5
h_i (mm)	0.3867	0.8	0.71	0.79
f (Hz)	500	2200	1200	2000
T (°C)	85	80	80	80

Table 2
Numerical and experimental T_{Ref} for the systems (A), (B) and (C).

System	(A)	(B)	(C)
T_{Ref}^{num} (°C)	85	80	80
T_{Ref}^{exp} (°C)	95	90	88

③ for the configuration (C). The length l_i and the thickness h_i of the blades, as well as the operating temperature T and the target frequency f of each blades are detailed in the Tab. 1.

The double-blade systems are therefore built from an analysis which considers each single-blade independently, without accounting for the coupling between blades. Figures 5(a), 5(b) and 5(c) show the variations of |R| in the complex frequency plane. The points noted k_i denote the zeros of R of the system k induced by the blade i. For comparison, the points noted S_i are the zeros of single-blade systems. The variations of R on the real frequency axis are shown in Figs. 5(d),(e),(f).

When the blades are designed for two frequencies that are far away from each other, the zeros of the dual-blade (B) almost correspond to the zeros of the two associated single-blades (see Fig. 5(b)). On the contrary, when the targeted frequencies are close to each other, the zeros of the dual-blade (C) no longer correspond to the zeros of the isolated single-blades (see Fig. 5(c)) and are thus no longer located on the real frequency axis. Both the frequencies and the amplitude of |R| are different (see Fig. 5(f)). This could be explained by a coupling effect between the two blades.

It can be noted, however, that it is possible to exactly reach zero at one of the two target frequencies by adjusting the temperature. Referring to the trajectory of the zero in Fig. 2(a), in order to locate C_1 on the real frequency axis, the temperature has to be lowered. Conversely, to locate C_3 on the real frequency axis, the temperature should be increased. Besides, it is possible to design a dual-blade system able to reach two critical couplings at close frequencies. This requires to account for the coupling between both blades in the parametric study, which is not addressed in this article. Although the perfect absorption at wide frequency range cannot be reached using this method, multi-blade systems are still relevant solutions for widening the damping frequency range of systems.

The three systems (A), (B) and (C) (see Figs. 1(d),(e),(f)) are manufactured in aluminum beams of length $L \approx 1$ m by wirecut electrical discharge machining. The layer of SMP is glued to each blade with epoxy glue. The beam is hanged with elastic wires (Fig. 1(g)) to mimic free boundary conditions. To ensure the most uniform thermal field possible, the beam is placed in a thermal chamber for the time of the measurements. To verify the effective temperature, a thermal controler (RKC REX-D100 with a precision of 0.1°C) is used with the sensor located near the SMP layer. The temperature regulation has been observed to be stable within a 1°C interval. The measurements are performed with a temperature step varying between 5°C and 0.5°C depending on the change of the mechanical properties of the SMP (the 0.5°C step was used close to the target temperatures). All measurements are started 2 minutes after temperature stabilization so that the temperature can be considered as uniform in the sample. This procedure has been successfully proven in previous works [16, 11, 26]. A voice-coil is used for the excitation to generate a white noise at $x = x_S$. The displacement field is measured at five positions x_i ($i \in [1 : 5]$) using accelerometers located between the excitation and the equipped end. Then, the contributions of the forward and backward propagating and evanescent waves amplitudes are identified using an inverse technique in order to estimate R [25].

The analytical results are compared with the experimental measurements in Figs. 5(g) to 5(p) for different SMP temperatures. The critical couplings expected in practice are not reached exactly at the same temperature as in simulation. T_{Ref} is used to refer to the temperature showing comparable numerical and experimental results. The

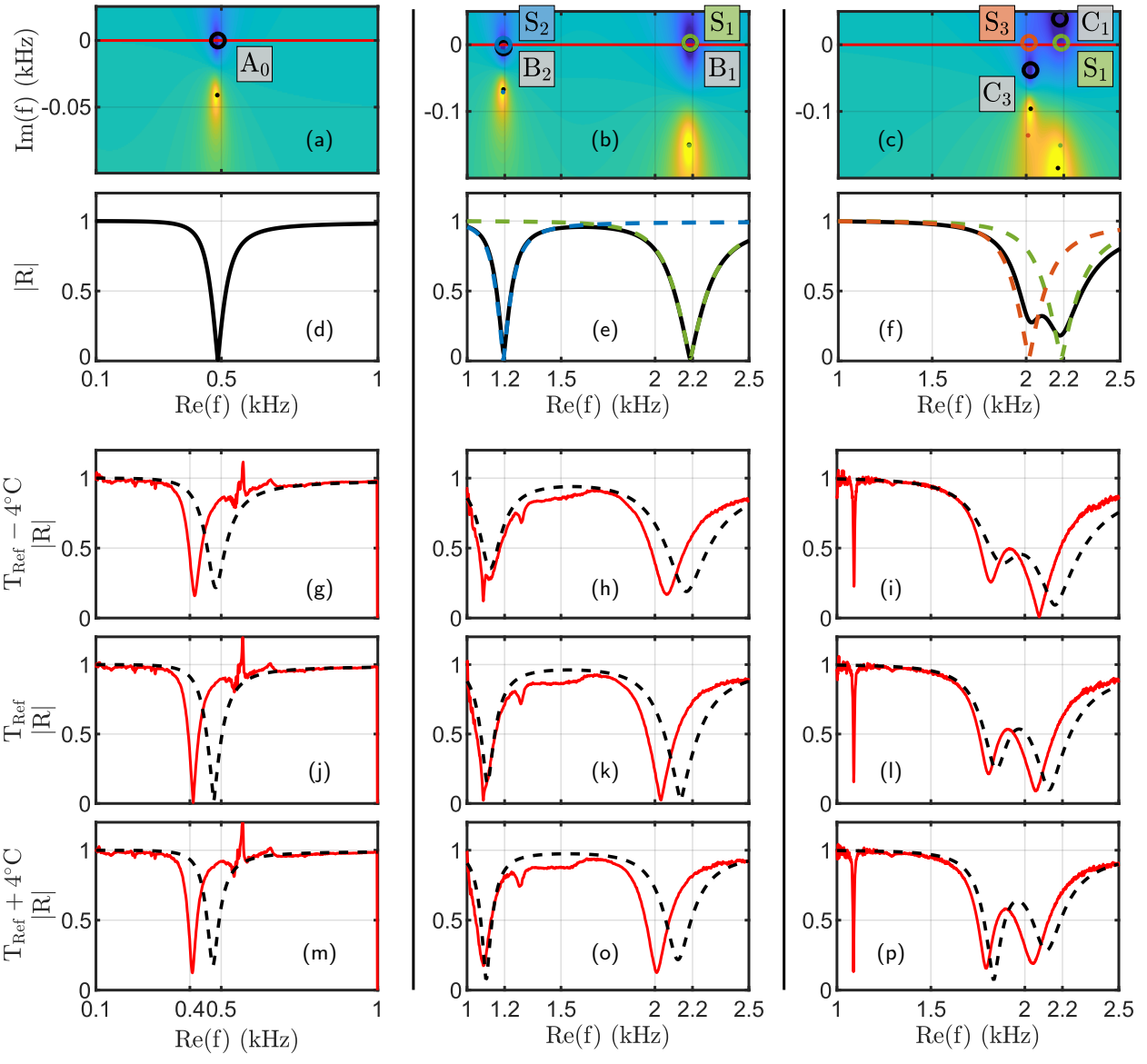

Figure 5: (a) log|R| in the complex frequency plane of the single-blade (A) at 85°C. The zero and pole are marked by the black circle and dot. The label A_0 names the zero induced by the blade 0 of the system (A). (d) |R| along the real frequency axis of the single-blade (A). (b) log|R| in the complex frequency plane of the dual-blade (B) at 80°C. The labels B_1 and B_2 denote the zeros induced by the blades 1 and 2 of the system (B). The color labels S_1 and S_2, marked with color circles, denote the position of the zero induced by the blade 1 and 2 of a two single-blades. (e) |R| along the real frequency axis of the double-blade (B) in black. The dashed color lines correspond to |R| of the compared single-blades. (c) and (f) same as (b) and (e) for the dual-blade (C) involving the blades 1 and 3. (g) to (p) present the measured |R| in red solid lines of the systems (A) (first column: (g), (j) and (m)), (B) (second column: (h), (k) and (o)) and (C) (third column: (i), (l) and (p)), compared to the numerical |R| in black dashed lines computed accounting for the machining geometry. In lines (i.e., (j), (k) and (l)) are the resulted |R| for different operating temperature around T_{Ref}, see Tab. 2.

difference between T_{Ref}^{num} and T_{Ref}^{exp} is about 10°C (see Tab. 2). However, a good trend can be observed in Fig. 5, in which the red curves show the experimental results and the dashed black curves show the numerical results accounting for the machining geometry errors of the blades (about 0.01 mm). The slight temperature-dependence of the elastic parameters of the aluminum is also considered [27]. The frequency offset can be explained by the thin layer of glue

and the added mass of the accelerometers which are not taken into account in the model. It can also be explained by the slight difference between the experimental parameters of the SMP and those obtained from the empirical model[16].

For system (A), the critical coupling is reached (see Fig. 5(j)). Around this reference temperature, it is clear that the trend is well captured experimentally (see Figs. 5(g),(m)). For system (B), the same conclusions as for (A) can be drawn. As expected, two critical couplings for two different frequencies are obtained (see Figs. 5(h),(k),(o)). For system (C), the same trends as in simulation are obtained (see Figs. 5(i),(l),(p)). The critical coupling can be reached on the first or the second drop by slightly decreasing or increasing the temperature. This is the case at 2.1 kHz for the second drop in Fig. 5(i). The drop at 1.1 kHz comes from a twisting mode.

5. Conclusion

The system proposed in this paper is a bending subwavelength resonator enhanced by thermal control. It provides a way to obtain a zero reflection at a target frequency by adjusting the length and thickness of a blade attached to a beam of given width and thickness. This blade is covered with a layer of SMP whose stiffness and damping properties depend on the temperature. It is a versatile system: if some parameters are constrained such as the geometry of the host beam or the thickness of the SMP layer, it is still possible to adjust the blade geometry to reach a target frequency. On the contrary, if the blade geometry is constrained, it is always possible to adapt the thickness of the SMP layer and play with the temperature.

In addition, we showed that it is possible to design a multi-resonant system by simply adding blade endings. The model presented is valid for more than two blades. It has been shown that these multiresonators are efficient in a homogeneous temperature environment as long as the blades are designed for this operating temperature. A nice way to improve the system would consist in designing a multiresonator where the temperature for each blade would be controlled independently. In this manner, it may be possible to achieve broadband perfect absorption, at least for some frequency ranges.

Acknowledgments

The work has been founded by the Agence Nationale de la Recherche in the framework of the project eTNAA (ANR-17-CE08-0035-01, 2017-2021). This work also has been supported by the EIPHI Graduate school (contract "ANR-17-EURE-0002"). Jean-Philippe Groby and Vicent Romero-García acknowlegde the financial support of the ANR-RGC METARoom (ANR-18-CE08-0021) project and the project HYPERMETA funded under the program Étoiles Montantes of the Région Pays de la Loire.

References

[1] David I. G. Jones. *Handbook of Viscoelastic Vibration Damping*. Wiley, 2001.

[2] X.Q. Zhou, D.Y. Yu, X.Y. Shao, S.Q. Zhang, and S. Wang. Research and applications of viscoelastic vibration damping materials: A review. *Composite Structures*, 136:460–480, 2016.

[3] J.Q. Sun, M.R. Jolly, and M.A. Norris. Passive, adaptive and active tuned vibration absorbers–a survey. *Journal of Mechanical Design*, 117:234–242, 1995.

[4] Steen Krenk and Jan Høgsberg. Tuned mass absorber on a flexible structure. *Journal of Sound and Vibration*, 333(6):1577–1595, 2014.

[5] Heng YUAN, Min WAN, and Yun YANG. Design of a tunable mass damper for mitigating vibrations in milling of cylindrical parts. *Chinese Journal of Aeronautics*, 32(3):748–758, 2019.

[6] Liang Sun, Ka Yan Au-Yeung, Min Yang, Suet To Tang, Zhiyu Yang, and Ping Sheng. Membrane-type resonator as an effective miniaturized tuned vibration mass damper. *AIP Advances*, 6(8):085212, 2016.

[7] Jacob Pieter Den Hartog. *Mechanical vibrations*. Courier Corporation, 1985.

[8] Antonio Carcaterra and Adnan Akay. Transient energy exchange between a primary structure and a set of oscillators: Return time and apparent damping. *The Journal of the Acoustical Society of America*, 115(2):683–696, 2004.

[9] A. Carcaterra, A. Akay, and C. Bernardini. Trapping of vibration energy into a set of resonators: Theory and application to aerospace structures. *Mechanical Systems and Signal Processing*, 26:1–14, 2012.

[10] Arnaldo Casalotti, Sami El-Borgi, and Walter Lacarbonara. Metamaterial beam with embedded nonlinear vibration absorbers. *International Journal of Non-Linear Mechanics*, 98:32–42, 2018.

[11] K. Billon, M. Ouisse, E. Sadoulet-Reboul, M. Collet, P. Butaud, G. Chevallier, and A. Khelif. Design and experimental validation of a temperature-driven adaptive phononic crystal slab. *Smart Materials and Structures*, 28(3), 2019.

[12] Guobiao Hu, Andrew C. M. Austin, Vladislav Sorokin, and Lihua Tang. Metamaterial beam with graded local resonators for broadband vibration suppression. *Mechanical Systems and Signal Processing*, 146:106982, 2021.

[13] J. Leng, F. Gautier, A. Pelat, R. Pico, J.-P. Groby, and V. Romero-Garcia. Limits of flexural wave absorption by open lossy resonators: reflection and transmission problems. *New Journal of Physics*, 21(5):053003, 2019.

[14] V. Romero-Garcia, G. Theocharis, O. Richoux, and V. Pagneux. Use of complex frequency plane to design broadband and sub-wavelength absorbers. *The Journal of the Acoustical Society of America*, 139(3395), 2016.

[15] J.-P. Groby, R. Pommier, and Y. Aurégan. Use of slow sound to design perfect and broadband passive sound absorbing materials. *The Journal of the Acoustical Society of America*, 139(4):1660–1671, 2016.

[16] P. Butaud, E. Foltête, and M. Ouisse. Sandwich structures with tunable damping properties: On the use of shape memory polymer as viscoelastic core. *Composite Structures*, 153:401 – 408, 2016.

[17] Pauline Butaud, David Renault, Benoît Verdin, Morvan Ouisse, and Gael Chevallier. In-core heat distribution control for adaptive damping and stiffness tuning of composite structures. *Smart Materials and Structures*, 29(6):065002, 2020.

[18] V.B. Georgiev, J. Cuenca, F. Gautier, L. Simon, and V.V. Krylov. Damping of structural vibrations in beams and elliptical plates using the acoustic black hole effect. *Journal of Sound and Vibration*, 330(11):2497 – 2508, 2011.

[19] V. Denis, A. Pelat, and F. Gautier. Scattering effects induced by imperfections on an acoustic black hole placed at a structural waveguide termination. *Journal of Sound and Vibration*, 362:56 – 71, 2016.

[20] Guillaume Raybaud, Adrien Pelat, Morvan Ouisse, and François Gautier. Zero reflections by a 1d acoustic black hole termination using thermally controlled damping. *Journal of Sound and Vibration*, 510:116282, 2021.

[21] Simon Félix and V Pagneux. Multimodal analysis of acoustic propagation in three-dimensional bends. *Wave Motion*, 36(2):157–168, 2002.

[22] B.R. Mace. Wave reflection and transmission in beams. *Journal of Sound and Vibration*, 97(2):237–246, 1984.

[23] M. Geradin and D.J. Rixen. *Mechanical Vibrations: Theory and Application to Structural Dynamics*. John Wiley & Sons, third edition edition, 2014.

[24] D. Ross, E.E. Ungar, and E.M. Kerwin Jr. Damping of plate flexural vibrations by means of viscoelastic laminae. *J.E.Ruzicka(Ed.), Structural Damping*, page 49–87, 1960.

[25] V. Denis, F. Gautier, A. Pelat, and J. Poittevin. Measurement and modelling of the reflection coefficient of an acoustic black hole termination. *Journal of Sound and Vibration*, 349:67 – 79, 2015.

[26] M. Ouisse, D. Renault, P. Butaud, and E. Sadoulet-Reboul. Damping control for improvement of acoustic black hole effect. *Journal of Sound and Vibration*, 454:63 – 72, 2019.

[27] E. G. Stanford. Le module d'young de l'aluminium et de ses alliages en fonction de la température [the young's modulus of aluminium and its alloys as a function of temperature]. *Rev. Met. Paris*, 51(10):674–678, 1954.